iScience

CellPress
OPEN ACCESS

Article

Growth of highly conducting $MoS_{2-x}N_x$ thin films with enhanced 1T′ phase by pulsed laser deposition and exploration of their nanogenerator application

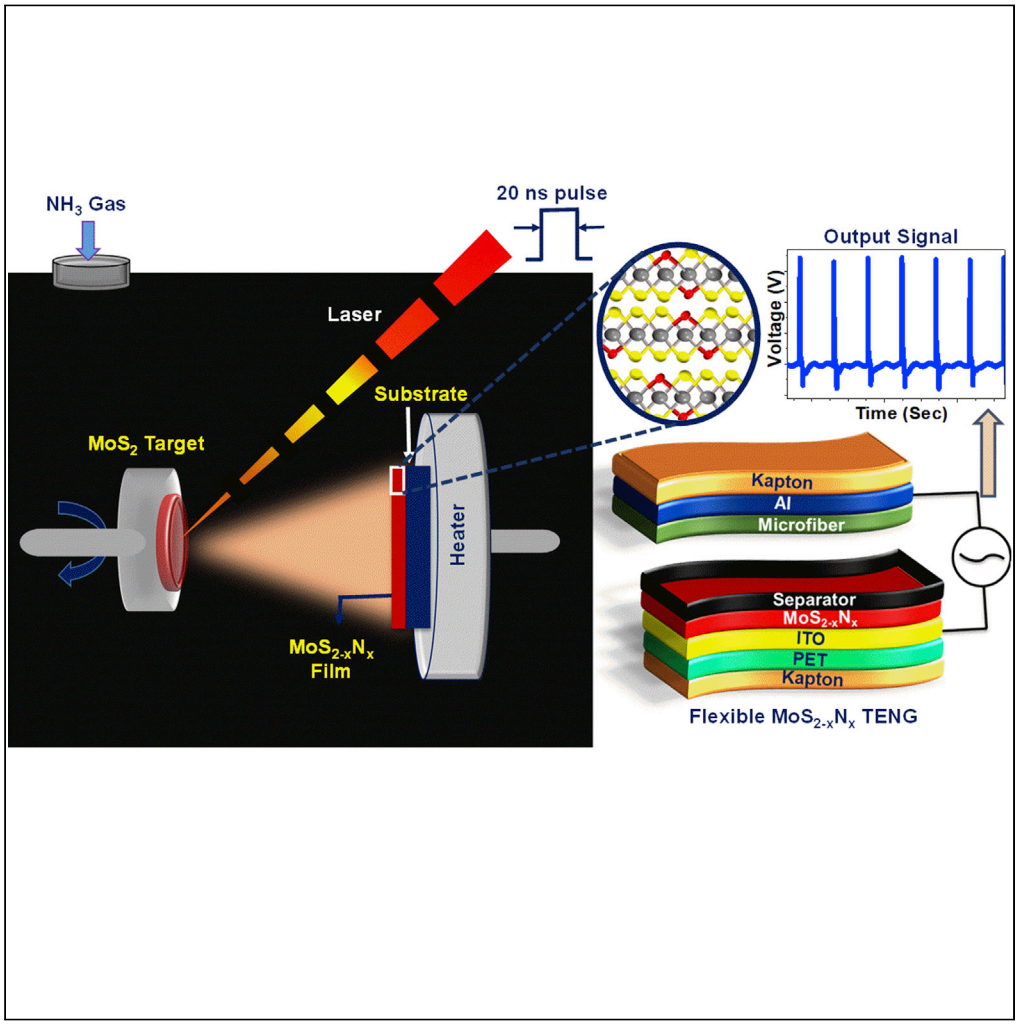

Swati Parmar, Neetu Prajesh, Minal Wable, Ram Janay Choudhary, Suresh Gosavi, Ramamoorthy Boomishankar, Satishchandra Ogale

satishogale@iiserpune.ac.in, satishogale@tcgcrest.org (S.O.)
boomi@iiserpune.ac.in (R.B.)

Highlights

$MoS_{2-x}N_x$ films grown on c-Al_2O_3 and ITO/PET by pulsed laser deposition in NH_3

p-type doping with high conductivity and 1T′+2H dual polymorph state is realized

Increased work-function of $MoS_{2-x}N_x$ films over pristine MoS_2 is realized

Impressive Triboelectric Nanogenerator application is demonstrated with $MoS_{2-x}N_x$

Parmar et al., iScience 25, 103898
March 18, 2022
https://doi.org/10.1016/j.isci.2022.103898

iScience

CellPress
OPEN ACCESS

Article

Growth of highly conducting $MoS_{2-x}N_x$ thin films with enhanced 1T′ phase by pulsed laser deposition and exploration of their nanogenerator application

Swati Parmar,[1] Neetu Prajesh,[2] Minal Wable,[1] Ram Janay Choudhary,[3] Suresh Gosavi,[4] Ramamoorthy Boomishankar,[2,*] and Satishchandra Ogale[1,5,6,*]

SUMMARY

High-quality growth of $MoS_{2-x}N_x$ films is realized on single-crystal *c*-Al_2O_3 substrates by the pulsed laser deposition (PLD) in ammonia rendering highly stable and tunable 1T′/2H biphasic constitution. Raman spectroscopy reveals systematic enhancement of 1T′ phase component due to the incorporation of covalently bonded N-doping in MoS_2 lattice, inducing compressive strain. Interestingly, the film deposited at 300 mTorr NH_3 shows ~80% 1T′ phase. The transport measurements performed on $MoS_{2-x}N_x$ films deposited at 300 mTorr NH_3 display very low room temperature resistivity of 0.03 mΩ-cm which is 100 times enhanced over the undoped MoS_2 grown under comparable conditions. A triboelectric nanogenerator (TENG) device containing biphasic $MoS_{2-x}N_x$ film as an electron acceptor exhibits a clear enhancement in the output voltage as compared to the pristine MoS_2. Device architecture, p-type N doping in MoS_2 lattice, favorably increased work-function, multiphasic component of MoS_2, and increased surface roughness synergistically contribute to superior TENG performance.

INTRODUCTION

Transition metal chalcogenides (TMCs) have rapidly acquired the status of technology materials of interest during the past decade because of their immensely interesting application-worthy physical properties (Jariwala et al., 2014)(Sebastian et al., 2021) (Barani et al., 2021) (Zhang et al., 2019)(Lee et al., 2017) (Briggs et al., 2019) (Mak et al., 2019), (Shin et al., 2012). Amongst the various materials belonging to this class, MoS_2 has perhaps been the most investigated one in recent years, a remarkable feature of MoS_2 being its intrinsic ability to support multiple polymorphs(Acerce et al., 2017). The polymorphs of MoS_2 afford wide bandgap tunability, with 1T′ phase being metallic and its polymorphs being metastable semiconductors with bandgap from <0.8 meV to 1.9 eV (Zhao et al., 2018). This aspect has brought MoS_2 to the center stage along with graphene and other 2D carbides and nitrides from the standpoint of both fundamental research and technological applicability.

Structurally, a monolayer of MoS_2 consists of a layer of three atoms in zigzag configuration, where one Mo atom is sandwiched between the two S atoms and the layers are stacked with very weak van der Waals forces. The primary polymorphs of MoS_2 are 1T (trigonal phase), 1H and 2H (hexagonal phase), and 3R (rhombohedral phase). Amongst these phases, the 1T phase is the least stable because of its thermodynamically metastable nature and tends to form the more stable 2H phase by reorganizing its stacking layers and geometry. The metastable 1T phase can also transform to other polymorph intermediates such as 1T′, 1T″, and 1T‴ via Jahn-Teller distortions (Zhao et al., 2018). Indeed, doping of octahedral and tetrahedral geometry in VDW in TMDCs drives several factors such as registry of interlayer stacked atoms, tilting of octahedrons, bond length, and bond angle, which cause structural distortions leading to the superlattices of $a_0 \times 2a_0$ dimer chain (1T′), $2a_0 \times 2a_0$ diamond shape (1T″) and $\sqrt{3}a_0 \times \sqrt{3}a_0$ trimerized clustering (1T‴) (Zhao et al., 2018). A well-established method of formation of 1T phase from 2H phase of MoS_2 is the alkali ion (Li^+, Na^+, and K^+) intercalation route.

Controllable *in-situ* doping of 2D materials is highly desirable for high-performing heterojunction devices to control the electronic structure, device parameters, and overall device functionality. In this regard, many strategies have been developed to enhance the MoS_2 electronic properties such as molecular

[1]Department of Physics and Centre for Energy Science, Indian Institute of Science Education and Research (IISER), Pune, Maharashtra 411008, India

[2]Department of Chemistry and Centre for Energy Science, Indian Institute of Science Education and Research (IISER), Pune, Maharashtra 411008, India

[3]UGC-DAE Consortium for Scientific Research, Indore 452001, India

[4]Department of Physics, Savitribai Phule Pune University, Pune, Maharashtra 411007, India

[5]Research Institute for Sustainable Energy (RISE), TCG Centre for Research and Education in Science and Technology (TCG-CREST), Kolkata 700091, India

[6]Lead contact

*Correspondence: satishogale@iiserpune.ac.in, satishogale@tcgcrest.org (S.O.), boomi@iiserpune.ac.in (R.B.)

https://doi.org/10.1016/j.isci.2022.103898

surface doping by oleylamine (Rosa et al., 2016), polyethylenimine (Du et al., 2013), and benzyl viologen (Kiriya et al., 2014) for effective electronic charge transfer (Tang and Jiang, 2015). Nevertheless, the non-covalent bonding behavior of these doped molecules is volatile, which makes it difficult to control the doping concentration over time and stabilize the desired phase(s). Doping of transition elements (Re, W, Pd, Cu, Co, Ni, Fe, Nb etc.) (Gao et al., 2020) (Fu et al., 2020), (Martinez et al., 2018), noble metal elements (Ag, Au and Pt) (Wang et al., 2019b), (Mombrú et al., 2018), non-metals (O, N, and Cl) (Yang et al., 2014) (Tang et al., 2020), (Azcatl et al., 2016) or vacancies (Mo and S) (Feng et al., 2014), as well as intercalation (Li, Na, and K) (Zou et al., 2020), (Liu et al., 2018) composite formation (MoS_2/Graphene, MoS_2/h-BN, etc) (Wang et al., 2019a), (Parmar et al., 2019) and substrate-induced strain effect (c-Al_2O_3, $SrTiO_3$, $LaAlO_3$ $SrLaAlO_4$, etc) (Parmar et al., 2021a), have been shown to greatly enhance the electronic properties of MoS_2. While MoS_2 is technically an intrinsic semiconductor, practical materials exhibit an n-type semiconductor character owing to the naturally present S vacancies (Zhang et al., 2021). This also hinders the realization of their bipolar nature for a variety of applications in the domain of electronics and optoelectronics, although some successes have been achieved in this context with interesting consequences. For instance, substituting Mo in MoS_2 lattice with Nb transforms the intrinsic n-type semiconducting behavior to p-type with increased hole density (3.1×10^{20} cm^{-3}) and high mobility (8.5 cm^2V^{-1} s^{-1}) (Das et al., 2015). Also, the growth windows of polymorphic TMCs using non-metal doping have so far remained relatively unexplored. Interestingly, N doping is one of the facile methods that greatly enhance the device performance by introducing finite and enhanced density of states at the Fermi-level, thereby providing high carrier concentration. For instance, Li at el. calculated that the introduction of 3% strain due to N doping in N-Mo-S lattice leads to 2H to 1T′and 2H to 1T phase transition because of geometrical changes, charge injection and strain (Li and Li, 2018).

The chemical vapor deposition method employed to dope TMD thin films requires toxic precursors, high temperatures, and also generates toxic by-products; and the growth of epitaxial film by this method is non-trivial (Frisenda et al., 2018). Mechanical and chemical synthesis protocols provide flaky forms, whereas chemical exfoliation requires intercalation of alkali metal ion or foreign element to synthesize the desirable 1T′ phase. This chemical synthesis route is also very time-consuming and requires further washing and processing to create an application-worthy thin film platform. Covalent doping via the substitution of metal and chalcogen atoms is a viable approach to achieve stable and controllable doping in these material systems.

Pulsed laser deposition (PLD) is a unique stoichiometry-transferring single-target thin film deposition technique that allows the growth of multi-functional, phase tunable, and stable thin-film growth, with the possibility of ambient control to achieve non-metal doping (with N, S, O) and pressure control to realize vacancy doping (Parmar et al., 2021b). The substrate temperature is another key parameter that can enable film quality, dopant, and defect control. Further, the PLD technique involves several laser-related process parameters such as laser energy density, pulse frequency, number of laser ablating shots, and so on. for film quality and thickness control (Wang et al., 2014) (Siegel et al., 2015) (Serrao et al., 2015), (Serna et al., 2016)

Ubiquitously, there are several ways to modify the intrinsic properties of materials for high performing TENG devices such as dielectric constant, work function, electrical poling, composites and chemical doping (Kim et al., 2020). Since MoS_2 is ranked higher in the negative triboelectric series, it has definitely become interesting to understand the triboelectric charging behavior of MoS_2 in TENG devices (Seol et al., 2018). The TENG output response is often associated with the effective work functions that govern the charging polarity of the materials, which can be effectively tuned by chemical doping (Kim et al., 2020). Seol et al. have reported that $AuCl_3$doped MoS_2 exhibits superior Voc in TENG as compared to benzyl viologen (BV)-doped MoS_2 because of their differences in work-functions which represent p-type and n-type chemical doping, respectively. The p-type $AuCl_3$ doped MoS_2 increases the effective work function, making it more electronegative in the triboelectric series, while the BV doping decreases the effective work-function of MoS_2 making it more tribo-positive and lowers the Voc (Seol et al., 2018). Thus, the p-type covalent N doping in MoS_2 was performed to increase the effective work-function of the $MoS_{2-x}N_x$ system. Here, we have used chemical doping toward manipulation of work function, type of charges, electron density, and bonding in N doped MoS_2which has been carefully examined by several characterizations, and its detailed analysis toward material intrinsic properties for TENG enhanced performance is presented.

Table 1. Obtained room temperature experimental phonon frequencies in Raman spectra of MoS_2 grown on c-Al_2O_3 under 300, 100, 10 mTorr, and pristine MoS_2 respectively

Phonon Mode	300 mTorr (cm^{-1})	100 mTorr (cm^{-1})	10 mTorr (cm^{-1})	MoS_2 (cm^{-1})
A_{1g}	~405.6	~406.2	~407.2	~407.5
E_{2g}	~376.1	~381.8	~381.4	~381.5
E_{1g}	~285.4	~287.1	~287.6	~288.2
J_1	~148.8	~151	–	–
J_2	~197, and ~222	~227	~225.4	~225.1
J_3	~333	~332	–	–

Here the intensities of the most intense (A_{1g}) peak are normalized.

The growth of $MoS_{2-x}N_x$ (anionic doping) thin films examined in this study was accomplished by employing NH_3-assisted PLD for *in-situ* N doping in MoS_2 lattice via laser-generated plasma. A comprehensive and rigorous analysis of Raman, XPS, VBS, and XANES spectra for the $MoS_{2-x}N_x$ deposited under 10, 100 and 300 mTorr NH_3 pressure reveals that substantial enhancement in the 1T′-phase component results for films grown at 300 mTorr NH_3 pressure. It can be attributed to the substitution of S with N forming its covalent bonding with the Mo atom. While the possibility of incorporation of some hydrogen cannot be ruled out, we did not find evidence of the same in the set of characterizations employed. The growth pressure also plays a key role in the tunability and stabilization of the 1T′ phase. Interestingly, the carrier transport properties also evolve rapidly as a function of doping rendering very high electrical conductivity in films grown at high (300 mTorr) ammonia pressure. We also examined the applicability of such highly nitrogen doped films for the triboelectric nanogenerator (TENG) device by growing them on flexible conducting ITO/PET substrate at 100 °C. Notably such films can be expected to be poly or micro-crystalline, yet the grains could be expected to preserve the virtues of the doping effects. Indeed, the device based on this material demonstrated impressive voltage/current output with the p-type property of the material getting reflected therein. It is important to note that the N doped MoS_2 material is in itself very interesting and is an important object of this study. Dry processing routes such as PLD are compatible with clean deposition environments and as such once proper growth parameters are identified, multilayer structures involving other metal oxides, sulfides and nitrides would be feasible. TENG application is used as a proof of concept to elucidate how the nitrogen doping could affect the involvement of such doped 2D material in a device configuration.

RESULTS AND DISCUSSIONS

Structural and surface characterization

The Raman spectra for N doped MoS_2 grown on single crystal c-Al_2O_3 (0001) substrate by using PLD in ammonia at pressures of 10, 100, and 300 mTorr are shown in Figure S1. All the spectra were normalized vis-á-vis the high-intensity A_{1g} phonon mode for better comparison, as this mode is present in all cases and is common for both the 1T′ and 2H phases of MoS_2. It is observed that the 300 mTorr film shows remarkably strong intensity for J_2, J_3, and E_{2g} phonon modes over the 10 and 100 mTorr cases; and the J_2 mode contribution gets smaller in the order of 300 mTorr > 100 mTorr>10 mTorr. All the observed Raman modes are tabulated in Table 1. Two distinct zone center first order sharp peaks at ~406 cm^{-1} and ~382 cm^{-1} corresponds to A_{1g} (out of plane) and E_{2g} (in-plane) modes, respectively, in the case of pristine MoS_2 and 300 mTorr grown $MoS_{2-x}N_x$ represent the 2H phase component (Figure 1A). The red-shift in the vibrational frequency in the doped film (Figure 1A, inset) can be attributed to the change in intra and intermolecular force constants of VDW MoS_2. The packing of MoS_2 lattice is affected by the external defects and dopants that change the intermolecular distances and hence the intermolecular force constants, resulting in the red shift of the A_{1g} phonon mode. Interestingly, the peak splitting of E_{2g} mode into and is significantly high in the 300 mTorr grown MoS_2 case, which corresponds to the symmetry breaking of the E_{2g} phonon mode because of N doping (Parmar et al., 2019). Further, a slight increase in FWHM in the doped system is due to the defect states reflecting the structural distortion(s). Interestingly, the disappearance of peak at ~287 cm^{-1} (resemble E_{1g} in-plane mode of 2H MoS_2) in 300 and 100 mTorr NH_3 case depicts the enhancement of 1T′ phase MoS_2 in the doped films. This implied that because of N doping in MoS_2 lattice, the structural distortion occurs that modifies the bond length and angle; and the structure of the 2H MoS_2 transforms from 2H to 1T′ phase, which modifies the electronic properties of the $MoS_{2-x}N_x$ film, as discussed in the later section.

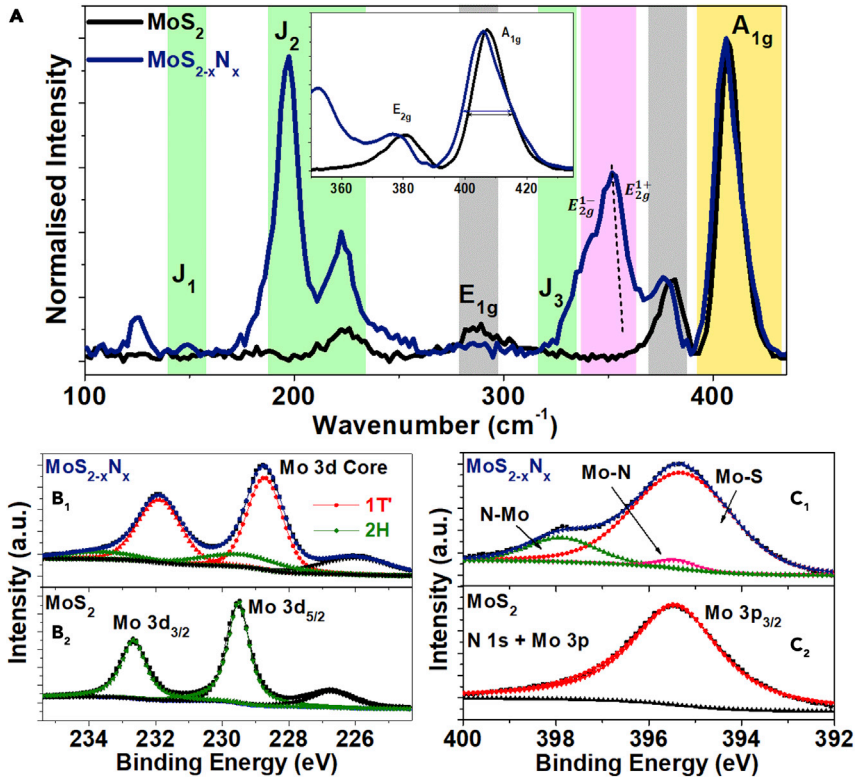

Figure 1. Raman and XPS Spectra of $MoS_{2-x}N_x$ thin-film grown on *c*-Al_2O_3 under 300 mTorr NH_3 pressure and of pristine MoS_2/*c*-Al_2O_3 case respectively

(A) Inset is the expansion of A_{1g} and E_{2g} mode from the frequency range 350–435 cm^{-1}. A significant enhancement of polymorphic J_2 mode and E_{2g} mode splitting corresponds to the co-existence of polymorph and enhanced doping concentration of N in MoS_2 lattice.

(B) X-ray photoelectron spectroscopy (XPS) of Mo 3*d* core for $MoS_{2-x}N_x$/*c*-Al_2O_3 (B_1) and for pristine MoS_2/*c*-Al_2O_3 (B_2).

(C) X-ray photoelectron spectroscopy (XPS) of N1s + Mo 3p core for $MoS_{2-x}N_x$/*c*-Al_2O_3 (C_1) and for pristine MoS_2/*c*-Al_2O_3 (C_2).

Ubiquitously, the key spectral signatures noted at 151 cm^{-1}, 196 cm^{-1}, 226 cm^{-1}, and 321 cm^{-1} correspond to the J_1, J_2, and J_3 modes for the 1T′ phase, respectively (Guardia et al., 2014). Here the atomic vibrations of Mo zig-zag chain correspond to J_1 and J_3 modes and the vibration of S atoms corresponds to the J_2 mode. The peak intensity for these modes can be seen to increase with the increase of NH_3 pressure and is exceptionally high for the film grown at 300 mTorr ammonia. The high-intensity peak at ~196 cm^{-1} (J_2) with the broad full-width half maximum (FWHM) represents the defect generated low frequency mode leading to the shortening of the distance between Mo-Mo zig-zag chains (Mignuzzi et al., 2015). Further, the splitting of J_2 phonon at ~197 and ~222 cm^{-1} can be understood in terms of the accommodation of compressive strain generated into the film due to N doping, leading to the formation of the distorted octahedron. The peaks at 125 and 150 cm^{-1} correspond to the combinatorial mode that arises because of the difference of A_{1g}–J_2 phonon modes (Ahmed et al., 2020). The significant enhancement in J_2 mode and appearance of J_1 and J_3 mode in 300 mTorr N-H:MoS_2 film can be attributed to the generation of compressive strain in the film as the atomic radius of N (65 p.m.) is much smaller as compared to S (100 p.m.). Another possibility of this doublet could be because of the formation of Mo-N bond in presence of high-pressure ammonia, and the vibrational frequency for the same also appears at 350 cm^{-1}, as reported in the literature (Azcatl et al., 2016). Thus, the $MoS_{2-x}N_x$ film deposited at 300 mTorr NH_3 perfectly fits the picture of the interlayer Mo-S, Mo-N, and intra-layer S-S, S-N, and possibly N-N interactions leading to the formation of high component of the 1T′ phase MoS_2.

The chemical structure and chemical components of pristine and doped MoS_2 were further studied by the XPS technique. Figures 1B_1, B_2 and 1C_1, C_2 display the XPS spectra of pristine MoS_2 and $MoS_{2-x}N_x$ (grown at 300 mTorr ammonia pressures) films. Based on previous reports (Yang et al., 2019), (Hu et al., 2018) N doped

MoS_2 (397-399 eV), MoN (395 eV), and Mo_2N (397 eV) related signatures correspond to specific Mo-N bonding/coordination. Therefore, the broad peak at around 397.3 eV observed in Figure 1C_2 can be assigned to Mo-N non-specific bonding. Further, the systematic shift toward the lower binding energy is found to be related to the increased doping concentration due to the increase in the NH_3 pressure from 10, 100, to 300 mTorr (Figures S2, S3, and S4). Therefore, it is important to calculate the concentration of N (N_c) in $MoS_{2-x}N_x$ lattice. We quantitatively calculated the N_c of the doped films grown at NH_3 pressures of 100 and 300 mTorr, and the corresponding values were found to be 18.5%, and 25%, respectively. This represents significant degree of nitrogen incorporation, more of an anionic alloy. The percentage was obtained by the ratio of integrated intensities of N 1s core to Mo $3d_{5/2}$ (Azcatl et al., 2016).

The doublet structure of the Mo 3d and S 2p spectra illustrated in Figures 1B_1, B_2 and 1C_1, C_2 reflect the characteristic spin-orbit splitting between Mo $3d_{3/2}$ and Mo $3d_{5/2}$ states at 232.6 and 229.5 eV respectively (Li et al., 2017), and for S $2p_{1/2}$ and S $2p_{3/2}$, states at 163.7 and 162.5 eV, respectively. The sharp peaks of Mo 3d core for pristine MoS_2 are indicative of the good local crystallinity of the samples. The shift of ~0.5 eV toward the lower binding energy of the doped system reflects the presence of polymorphism due to N doping and consequent possible decrease in the effective charge state of Mo. The defective structure with non-metal dopants causes displacement of the Mo^{4+} 3d peaks toward the lower binding energies in the Mo 3d spectra (Pal et al., 2017). The percentage of 1T′ and 2H was also been calculated by assigning the peak in regions 229 and 232 eV, as shown in Figure 1B_1, B_2. The 300 mTorr case shows significantly higher fraction of (~80%) 1T′ phase of MoS_2, which is the metallic phase. Notably, the peak at 229.5 eV also corresponds to the Mo-N bonding which is at about the same location as that of Mo-S bonds of 2H phase MoS_2 (Azcatl et al., 2016). Therefore, this XPS signature will also have the corresponding Mo-N contribution in 100 and 300 mTorr cases that cannot be neglected. Similarly, in Figure 1C_2 the consecutive shift toward the lower binding energy in S $2p_{1/2}$ and $2p_{3/2}$ spin-orbit splitting for 100 and 300 mTorr MoS_2 films again reflects the enhancement of 1T′ phase with the increase of dopant concentration. All the peaks were corrected with the reference binding energy of C (Figure S5). All these results indicate that the doping of non-metals brings about dramatic microstructural changes and the modification of strain state by altering the bond lengths and bond angles.

AFM and HRTEM characterisation

The atomic force microscopic (AFM) topography in Figures S6A and S6B shows the increase in mean roughness from 2.78 nm to 5.2 nm in $MoS_{2-x}N_x$ over pristine MoS_2. In order to get an idea about the local structure development during initial film growth, we recorded High-resolution transmission electron microscopy (HRTEM) images on ultrathin films of MoS_2 and $MoS_{2-x}N_x$ deposited directly on carbon-coated holy grids by giving only 30 shots *at room temperature*. It may be noted that these data do not correspond to the films grown at higher temperature which are expected to be structurally far superior on larger length scales. The pristine MoS_2 film was prepared under Ar atmosphere, whereas the $MoS_{2-x}N_x$ film was deposited under 300 mTorr NH_3 atmosphere. It is very clear from the obtained FFT image (Figures S7A and S7B) that the pristine MoS_2 has common honeycomb lattice corresponding to the 2H phase, whereas the co-existence of 1T′ and 2H phases is evident in the case of the $MoS_{2-x}N_x$ film, with trigonal lattice reflecting the 1T′ phase.

XANES characterization

The X-ray absorption near edge spectra (XANES) is a powerful tool to reveal microstructural details and electronic information on metal coordination sites. The formation of $MoS_{2-x}N_x$ species under NH_3 pressure was therefore confirmed by synchrotron-based XANES. We have analyzed the N K-edge, Mo M-edge, and S L-edge of $MoS_{2-x}N_x$ films and the Mo and S edges for the pristine MoS_2 films grown on *c*-Al_2O_3. The Nitrogen K-edge X-ray absorption energy is about 400 eV (Figure 2A), and the main absorption edge is observed at ~405 eV (Reinholdt et al., 2021). Importantly, the Mo M_3-edge also occur at ~400 eV that arises from 3p→4d transition (George et al., 2009), (Lajaunie et al., 2015) The substantially enhanced intensity of the near 400 eV signature in the case of $MoS_{2-x}N_x$ as compared to pristine MoS_2 suggests addition of the Mo N and N K edge contributions. Further, in S $L_{2,3}$-edge the spin orbit splitting occur in the range of 164–168 eV, as shown in Figure 2B (George et al., 2009). In addition, a comparative analysis based on the observed shape, peak area, and intensities provides information on the local bonding environment responsible for M edge, N edge, and L edge positions (Cai et al., 2015). The shoulder peak in N K-edge indicates that there is substantially extended energy states distribution which corresponds to Mo 4d electrons in the $MoS_{2-x}N_x$ case, further indicating the incorporation of the 1T′ phase in $MoS_{2-x}N_x$ (Cai et al., 2015; Lajaunie et al., 2015). According to the crystal field theory (CFT), the 2H semiconductor MoS_2 is

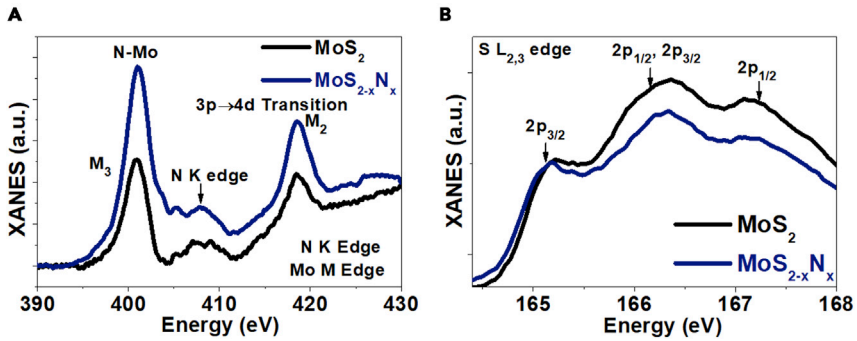

Figure 2. X-ray near edge spectra for $MoS_{2-x}N_x$ films grown on *c*-Al_2O_3 substrate

(A) N, K edge and Mo M edge are depicted from 390 to 430 eV.

(B) S L-edge XANES in the range of 164–168 eV energy.

due to the symmetry-induced splitting of Mo 4d orbitals of MoS_6 D_{3h} group into fully occupied Mo $4d_{z2}$, Mo $4d_{xy}$, Mo $4d_{x2-y2}$, and unoccupied Mo $4d_{xz}$ and Mo $4d_{yz}$ (Zhao et al., 2018). On the other hand, in the case of 1T′ MoS_2 semi-metallic character stems from the octahedral splitting of 4d orbital into triple triple-degenerate t_{2g} (d_{xy}, d_{xz}, d_{yz}) and double-degenerate e_g sets, with the t_{2g} orbitals partly occupied by the two 4d electrons. The N K-edges also reflects the high content of N in the $MoS_{2-x}N_x$ case. From the S L edge, it is divulged that in the $MoS_{2-x}N_x$ case, the feature at 166.5 eV arising because of the transition between S 2p to S 4d hybridized with Mo 5p states, is broadened and comprises two features. The additional feature compared to undoped MoS_2 indicates the mixing of S 4d and N 2p states via Mo 5p states. The lower content of S in the $MoS_{2-x}N_x$ case due to N substitution over pristine MoS_2 is clearly seen from the drop in intensity of the S $L_{2,3}$-edge (Figure 2B). (Cai et al., 2015) The above observations corroborate well with the noticeable changes in the electronic band structure due to the formation of 1T′ phase upon N doping in MoS_2 lattice.

Work-function and valance band maxima (UPS and VBS)

The work function values of $MoS_{2-x}N_x$ and pristine MoS_2 films were measured by UV photoelectron spectroscopy. The work function (Φ) of the heterostructures is calculated by:

$$\Phi = h\nu - E_{onset} \quad \text{(Equation 1)}$$

where $h\nu$ = 21.22 eV is the incident photon energy and E_{onset} is the onset energy of the secondary electrons obtained from the extrapolation of the slope drawn at the leading edge of the spectra to the baseline as shown in Figure 3A. From the equation, the work functions were estimated to be 4.67 and 4.85 eV for MoS_2/*c*-Al_2O_3 and $MoS_{2-x}N_x$/*c*-Al_2O_3 respectively. (Tao et al., 2014) The covalent N doping in MoS_2 lattice effectively engineers the work-function. The n-type behavior of pristine MoS_2 is attributed to sulfur vacancies and its significant depletion by N doping in the case of $MoS_{2-x}N_x$ films can cause the enhancement of the work function.

The hybridization of Mo 4d and S 3p orbitals leads to the formation of valance band states. In 2H MoS_2, the conduction band and valance band are mainly composed of Mo 4d orbitals. The noticeable Mo 4d states across the Fermi energy in $MoS_{2-x}N_x$ suggests the formation of 1T′ MoS_2 and hence with more conducting nature. Figure 3B compares the VBS spectra of $MoS_{2-x}N_x$/*c*-Al_2O_3 grown at 300 mTorr and pristine $MoS_{2-x}N_x$/*c*-Al_2O_3case. Figure S8 compares the same for different pressures. The extraction of the Valance band maxima (VBM) positions was done by taking the intersection of the linear extrapolation of the prominent edge in VBS spectra. The electronic states at ~1.8 eV belong to the Mo $4d_{z2}$ band of 2H MoS_2 which is below the Fermi energy, implying the intrinsic n-type doping. The well-established hybridization of Mo 4d and S 3p suggests the long-range in-plane ordering of MoS_2. (Tao et al., 2015) The progressive shift in the valence band edge toward the Fermi energy with increase of NH_3 growth pressure suggests the change in the electronic structure. For $MoS_{2-x}N_x$/*c*-Al_2O_3 grown at 300 mTorr the observed VBM position is located at −0.1 eV with reference to the Fermi energy rendering finite density of states at E_F and hence higher conductivity. This comes about by the increased 1T′ component with the nitrogen doping concentration. The

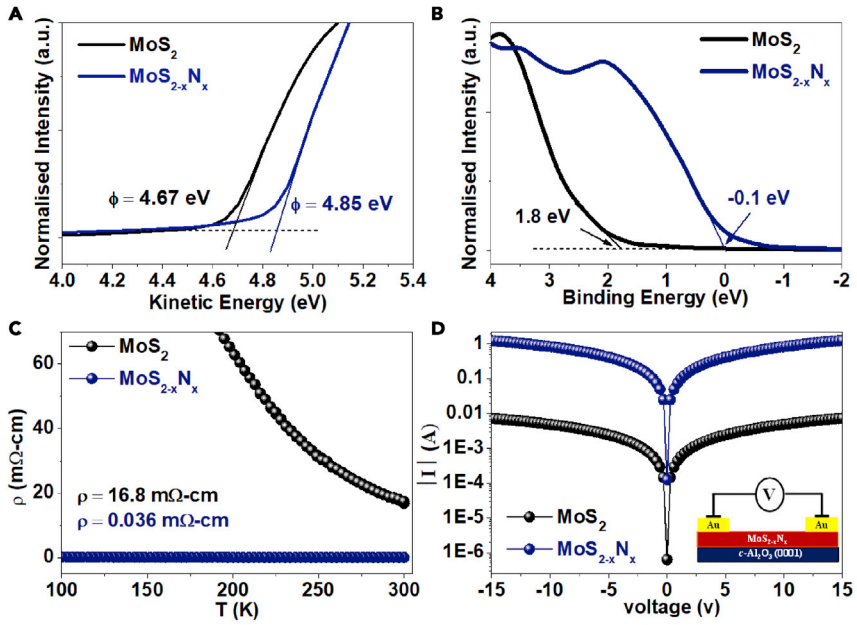

Figure 3. Electronic property exploration by UV photoelectron spectroscopy, valance band maxima, temperature dependent-resistivity and I-V characteristics of pristine MoS_2 and $MoS_{2-x}N_x$ films grown on *c*-Al_2O_3

(A) Secondary electron cutoff vs kinetic energy plot for work function calculation.

(B) Valance band spectra of pristine MoS_2 and $MoS_{2-x}N_x$; films grown on *c*-Al_2O_3, representing the Fermi-level overlapping for $MoS_{2-x}N_x$ (300 mTorr NH_3 pressure).

(C) Temperature-dependent carrier transport of 20 nm MoS_2 and $MoS_{2-x}N_x$ films grown on *c*-Al_2O_3 (0001) substrate, resistivity shows a highly conducting nature of $MoS_{2-x}N_x$ at room temperature.

(D) I-V characteristics of Au/MoS_2/*c*-Al_2O_3 and Au/$MoS_{2-x}N_x$/*c*-Al_2O_3 heterostructure.

binding energy of S 2p, Mo 3d and N 1s core (primary peaks), along with work-function and VBM of MoS_2/*c*-Al_2O_3 and $MoS_{2-x}N_x$/*c*-Al_2O_3 films are tabulated for comparison in Table 2.

Electronic transport properties (resistivity and I-V characteristics)

Doping of 2D materials often leads to new phenomena and is often considered as a proposition to enhance the electronic transport properties. Specifically, enhancing the electrical conductivity of MoS_2 films by doping is always interesting for enhancing its potential application-worthiness. Heavy doping can even cause significant changes to the band edges and work function, thereby boosting the functionality. Because our doped film consist of a high content of 1T′ phase rendered by N substitution at the sulfur site, the investigation of electrical transport is very interesting in this case. Indeed, the temperature-dependent in-plane four-probe resistivity measurement on 300 mTorr grown $MoS_{2-x}N_x$ thin-film shows an extremely (by a factor of about 500) low room temperature resistivity as compared to that of pristine (undoped) MoS_2 film. Because we used different NH_3 pressures to grow the films leading to differing N doping concentrations, the intra-atomic interaction and the degree of covalent bonding between N and Mo should differ, leading to distinct differences in the d-electron hopping (Parmar et al., 2019), (Park et al., 2015) We measured the electrical resistivity of $MoS_{2-x}N_x$ thin films comprising >80% 1T′+20% 2H phase and pure 2H MoS_2 phase film on *c*-Al_2O_3. The data over the 200–300 K regime are plotted and compared in Figure 3C. Indeed, the room temperature resistivity (ρ) shows much-enhanced conductivity for the $MoS_{2-x}N_x$/*c*-Al_2O_3 (0001) thin films (~0.036 mΩ-cm) with respect to the pristine 2H phase MoS_2/*c*-Al_2O_3 (0001) thin films (~16.8 mΩ-cm). Further, the pressure dependent comparison of T-dependent carrier transport of pristine MoS_2/*c*-Al_2O_3 (0001) and $MoS_{2-x}N_x$/*c*-Al_2O_3 (0001) deposited under different NH_3 pressure (10, 100, and, 300 mTorr) depicts the lowest resistivity in the 300 mTorr case (Figure S9). It is quite interesting that although the mixed-phase film shows >80% 1T′ phase (which is much above the percolation threshold), it does not show a fully metallic (i.e., decrease in resistivity while lowering the temperature) feature. Because it contains <20% 2H phase (dielectric proximity), electron localization in the semiconducting regions (along with grain boundary scattering effects) may be the contributing factor for this observation.

Table 2. Obtained binding energies for MoS_2 and $MoS_{2-x}N_x$ films grown on c-Al_2O_3 substrate

	MoS_2/c-Al_2O_3	$MoS_{2-x}N_x/c$-Al_2O_3
S $2p_{3/2}$	~162.5 eV	~162.1 eV
Mo $3d_{5/2}$	~229.5 eV	~228.7 eV
N 1s	–	~397 eV
Work-function	~4.67 eV	~4.85 eV
Valance band maxima	~1.8 eV	~–0.13 eV

The low-temperature resistivity data can be best fitted with the Mott-variable range hopping (Mott-VRH) model (i.e. ln $\sigma \propto 1/T^{1/(d+1)}$) where σ is the conductivity and d the dimension, signifying the important role of Anderson localization due to intrinsic disorder effect (possible structural defects, vacancies, and dislocations to lower the strain energy) for this insulating-like behavior (Figure S10) (Cho et al., 2021), (Zhou et al., 2016) In addition, much lower activation energy of $MoS_{2-x}N_x$ (~30.6 meV) is observed over that of pristine MoS_2 (~91.3 meV) (Figure S11) which also indicates the modification in the electronic correlation and consequent enhancement in electrical conductivity (Mitterreiter et al., 2021). Moreover, reported theoretical calculations reveal that the structural distortion-induced changes in crystal field splitting opens up a gap of ~100 meV for the semiconducting 1T′ phase (Pal et al., 2017).

In addition, we have also examined the I-V characteristics of heavily doped $MoS_{2-x}N_x$ thin films and compared the current with respect to pure 2H MoS_2 film. The in-plane current was measured across Au/$MoS_{2-x}N_x$ and Au/MoS_2 interfaces on the application of $\pm$15 V sweep voltage (Figure 3D). The channel length was kept ~0.6 μm between the two Au contacts. It is important to note here that the doped films show three order enhancement in the current as compared with pristine 2H MoS_2. This can be attributed to the fact that the enhancement in the 1T′ phase via covalent doping provides a smooth electronic transport through the grain boundaries. Generally, the transport in the polymorphic MoS_2 is driven by the tunneling of electrons and percolation from the metal-semiconductor grain boundaries of the 1T′ phase and 2H phase. However, the highly doped system provides a uniform 1T′ channel with pertinent electronic transport across the electrode.

Triboelectric nanogenerator performance

VDW-based TENGs represent an interesting mechano-electronic device (Lim et al., 2019). Herein, each VDW layer acts as an active electrode layer toward inter- and intra-layer charge generation and transfer. The strong interlayer coupling in VDW plays an important role in the charge generation/transfer. With the incorporation of defects, dopants, and charge distributions, this device functionality can be interesting and could generate superior performance. We therefore fabricated a TENG device using $MoS_{2-x}N_x$ and pristine MoS_2 films as an active material electrode in a vertical contact separation mode TENG design. A 20 nm film was coated on ~1.3 × 1.3 cm^2 area ITO/PET for this purpose. A 1-mm thick 3M double-sided tape boundary was used to maintain a distance between the top and bottom layers as depicted in Figure 4A. The MoS_2 or $MoS_{2-x}N_x$ film on ITO coated PET and microfiber separator in the middle were assembled with the aluminum tape upside down as top contact (Figure 4A) where the microfiber is composed of cellulose, a commercially available microfiber paper (α-cellulose content >98%) which is an environmentally friendly material. The device was laminated with a Kapton tape allowing some space for electrode connections to prevent damage to the device from the external environment. Then the Cu wires were soldered to the conducting sides of the top and bottom electrodes. A mechanical input of 10 N (measured by PASCO force sensor) was applied at 21 Hz frequency. During measurement, the Cu wires were connected to the oscilloscope to record the open-circuit voltage. A remarkably enhanced open-circuit value obtained for the pristine MoS_2 and $MoS_{2-x}N_x$ is in the ratio of ~1:3. The obtained peak to peak voltages were ~0.8 and ~2.7 V for pristine MoS_2 and $MoS_{2-x}N_x$, respectively (Figure 4B). The enhanced V_{oc} in doped films can result from polymorphism with high 1T′ component and very high electrical conductivity. The peak-to-peak voltage and current density were also calculated to obtain the overall $MoS_{2-x}N_x$ TENG efficacy under application of different external loads of 0.1, 0.4, 0.8, 1, 10, 20, 30, and 40 MΩ resistance (Figure S12) and the corresponding signal is shown in Figure S13. It is to be noted here that the asymmetric behavior in alternating output voltage in the vertical contact-separation mode can be observed because of the lower charge pushing from one to another electrode (Chen et al., 2020). In this mode when the upper electrode separates, the voltage is mainly associated with the dielectric film. Thus, the output voltage is much higher

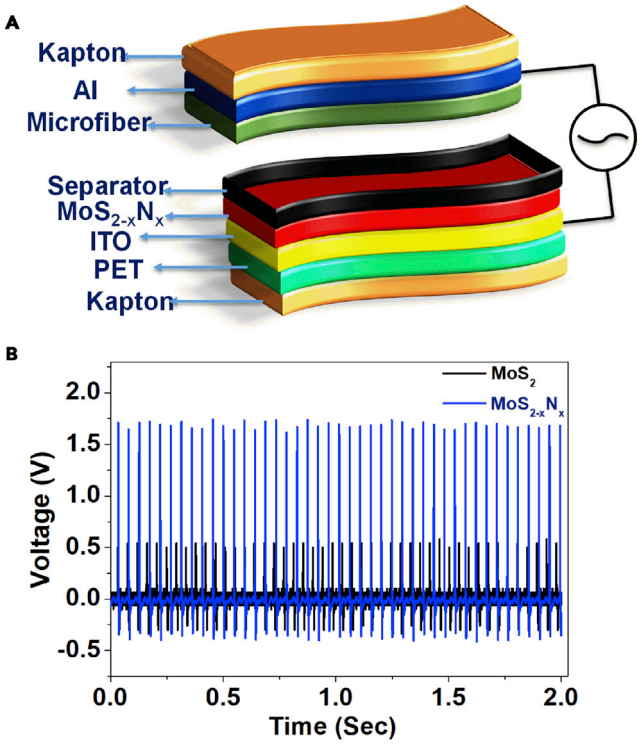

Figure 4. Triboelectric nanogenerator device architecture and output voltage performance of $MoS_{2-x}N_x$ and pristine MoS_2TENG

(A) Schematic of a TENG device containing $MoS_{2-x}N_x$ film grown on flexible ITO coated PET substrate.

(B) The continuous open-circuit voltage (V_{oc}) of $MoS_{2-x}N_x$ and pristine MoS_2 TENG devices was recorded at 21-Hz frequency.

in the upper electrode than the former electrode. The power density was also obtained to realize the net output powering capability of TENG for the different sets of loads (Figure S14). Figure S15 shows the cross-section FESEM image of $MoS_{2-x}N_x$ films grown on a flexible ITO-coated PET substrate.

Cellulose fibers are bio-degradable, lightweight, and high strength materials and have a high propensity to lose an electron because of the presence of abundant oxygen atoms, making it a prominent material for a tribo-positive layer (Chen et al., 2020). Here, the effective work-function of the MoS_2 and $MoS_{2-x}N_x$ films was calculated via UV photoelectron microscopy, which was the main factor for deciding upon its use in the triboelectric charging behavior. It is observed that the $MoS_{2-x}N_x$ films exhibit higher effective work function as compared to pristine MoS_2 film. Thus, the p-type Nitrogen doping in MoS_2 leads to the enhancement of work-function making it more negative in the triboelectric series. Thus, the triboelectric charging features are successfully modified by N doping in the MoS_2 lattice that change the effective work-function.

Under the application of external impulse-force, the physical contact between $MoS_{2-x}N_x$/microfiber/Al is instantly established and contact charging occurs. While triboelectricity basically embodies the contact charging process, the charge transfer has to take place between the two interfacing materials to generate a voltage across and drive currents across. This intrinsically involves their propensity to give and accept the charge; a consideration that lays the foundation for the existence of the triboelectric series. Moreover, because the currents have to flow through the bulk for compensating the charge imbalances resulting from the contact charging, the electronic band structures of the participating materials also come into play. There are situations where the electronic character of the two materials differs by way of being a metal, semiconductor, or insulator and this causes further complications of electronic currents and depolarization currents. Thus, the whole process is rather complex to elucidate in simple terms. In our case, the microfiber and Al hold different triboelectric polarity. When both the layers brought into contact, the electrons are exchanged the effective differential work function. Thus, the $MoS_{2-x}N_x$ TENG performance

enhancement over pristine MoS_2 TENG can be attributed to the synergy of the device architecture, p-type N doping in MoS_2 lattice, favorably increased work-function, multiphasic component of MoS_2 with enhanced conducting component 1T′ and increased surface roughness enhancing the trapped charge kinetics via locally enhanced field.

Conclusion

In summary, we report on the growth, properties, and applicability of high-quality thin films of $MoS_{2-x}N_x$ on single-crystal *c*-Al_2O_3 substrates under ammonia ambient by the pulsed laser deposition (PLD) technique. We find that the films exhibit 1T′/2H biphasic constitution, with the 1T′ component increasing dramatically with enhanced growth pressure of ammonia (~80% 1T′ phase @ 300 mTorr growth pressure). Raman characterization reveals that the enhancement of the 1T′ phase component can be attributed to the incorporation of covalently bonded N in the MoS_2 lattice inducing compressive strain. Transport measurements show progressive drop in resistivity with enhanced ammonia growth pressure and the $MoS_{2-x}N_x$ films grown at 300 mTorr NH_3 show extremely low room temperature resistivity of 0.03 mΩ-cm which is two orders of magnitude lower than the undoped MoS_2. In a triboelectric nanogenerator (TENG) device the biphasic $MoS_{2-x}N_x$ film grown at 300 mTorr NH_3 pressure serves as an electron acceptor and exhibits a 3-fold enhancement in the output voltage as compared to the pristine MoS_2. Increased work-function due to highly conducting covalent p-type N doping in multiphasic MoS_2 with increased roughness and device assembly synergistically contributes to this superior TENG performance.

Limitations of the study

In this study, we have fabricated, optimized, and characterized $MoS_{2-x}N_x$ films using pulsed laser deposition (PLD) in NH_3 ambient. In addition, we have elucidated the role of N in the MoS_2 lattice, which is responsible for enhancing its electronic properties via modulating the chemical and structural properties. While the possibility of incorporation of some hydrogen cannot be ruled out during the deposition in NH_3-assisted PLD, we did not find evidence of the same in the set of characterizations employed. However, a solid-state Nuclear Magnetic Resonance (NMR) can possibly bring out the role of Hydrogen in the $MoS_{2-x}N_x$ lattice, as H bonding can contribute to the changes of the electronic bands. Also, PLD is difficult to scale up; therefore, after the basic results are established by PLD studies, one could perform a follow-up with scalable sputtering or PVD techniques.

STAR★METHODS

Detailed methods are provided in the online version of this paper and include the following:

- KEY RESOURCES TABLE
- RESOURCE AVAILABILITY
  - Lead contact
  - Materials availability
  - Data and code availability
- EXPERIMENTAL MODEL AND SUBJECT DETAILS
- METHOD DETAILS
  - $MoS_{2-x}N_x$ thin-film growth
  - Structural and chemical characterizations
  - Electrical characterization
  - Nanogenerator output performance
- QUANTIFICATION AND STATISTICAL ANALYSIS
- ADDITIONAL RESOURCES

SUPPLEMENTAL INFORMATION

Supplemental information can be found online at https://doi.org/10.1016/j.isci.2022.103898.

ACKNOWLEDGMENT

Swati Parmar would like to thank CSIR for SRF fellowship. Satish Ogale and R. Boomishankar would like to thank DST Nanomission Thematic unit project (SR/NM/TP/13/2016) for funding support. We would like to thank Prof. Surjeet Singh and Ms. Dibyata Rout for providing the facility for the R-T measurement.

AUTHOR CONTRIBUTIONS

S.*P. and* S.O. developed the idea and design the experiments, S.P. performed and analyzed the thin film growth, characterization, and device fabrication. N.P. carried out the TENG device testing and B.R. helped with the analysis. M.W. helped in the FESEM characterization. R.C. helped in providing the XANES experiment and analysis. S.P. and S.O. co-wrote the paper. All the authors contributed to the discussion and analysis.

DECLARATION OF INTERESTS

The authors declare no competing interests.

Received: October 6, 2021
Revised: January 15, 2022
Accepted: February 5, 2022
Published: March 18, 2022

REFERENCES

Acerce, M., Akdoğan, E.K., and Chhowalla, M. (2017). Metallic molybdenum disulfide nanosheet-based electrochemical actuators. Nature *549*, 370–373.

Ahmed, T., Bellare, P., Debnath, R., Roy, A., Ravishankar, N., and Ghosh, A. (2020). Thermal history-dependent current relaxation in hBN/MoS_2 van der Waals dimers. ACS Nano *14*, 5909–5916.

Azcatl, A., Qin, X., Prakash, A., Zhang, C., Cheng, L., Wang, Q., Lu, N., Kim, M.J., Kim, J., Cho, K., et al. (2016). Covalent nitrogen doping and compressive strain in MoS_2 by remote N_2 plasma exposure. Nano Lett. *16*, 5437–5443.

Barani, Z., Kargar, F., Ghafouri, Y., Ghosh, S., Godziszewski, K., Baraghani, S., Yashchyshyn, Y., Cywiński, G., Rumyantsev, S., Salguero, T.T., et al. (2021). Electrically insulating flexible films with quasi-1D van der Waals fillers as efficient electromagnetic shields in the GHz and sub-THz frequency bands. Adv. Mater. *33*, 2007286.

Briggs, N., Subramanian, S., Lin, Z., Li, X., Zhang, X., Zhang, K., Xiao, K., Geohegan, D., Wallace, R., Chen, L.-Q., et al. (2019). A roadmap for electronic grade 2D materials. 2D Mater. *6*, 022001.

Cai, L., He, J., Liu, Q., Yao, T., Chen, L., Yan, W., Hu, F., Jiang, Y., Zhao, Y., Hu, T., et al. (2015). Vacancy-induced ferromagnetism of MoS_2nanosheets. J. Am. Chem. Soc. *137*, 2622–2627.

Chen, A., Zhang, C., Zhu, G., and Wang, Z.L. (2020). Polymer materials for high-performance triboelectric nanogenerators. Adv. Sci. *7*, 2000186.

Cho, C., Wong, J., Taqieddin, A., Biswas, S., Aluru, N.R., Nam, S., and Atwater, H.A. (2021). Highly strain-tunable interlayer excitons in MoS_2/WSe_2heterobilayers. Nano Lett. *21*, 3956–3964.

Das, S., Demarteau, M., and Roelofs, A. (2015). Nb-doped single crystalline MoS_2 field effect transistor. Appl. Phys. Lett. *106*, 173506.

Du, Y., Liu, H., Neal, A.T., Si, M., and Ye, P.D. (2013). Molecular doping of multilayer MoS_2field-effect transistors: reduction in sheet and contact resistances. IEEE Electron.Device Lett. *34*, 1328–1330.

Feng, L.-P., Su, J., and Liu, Z.-T. (2014). Effect of vacancies on structural, electronic and optical properties of monolayer MoS_2: a first-principles study. J. Alloys Compd. *613*, 122–127.

Frisenda, R., Navarro-Moratalla, E., Gant, P., Pérez De Lara, D., Jarillo-Herrero, P., Gorbachev, R.V., and Castellanos-Gomez, A. (2018). Recent progress in the assembly of nanodevices and van der Waals heterostructures by deterministic placement of 2D materials. Chem. Soc. Rev. *47*, 53–68.

Fu, S., Kang, K., Shayan, K., Yoshimura, A., Dadras, S., Wang, X., Zhang, L., Chen, S., Liu, N., Jindal, A., et al. (2020). Enabling room temperature ferromagnetism in monolayer MoS_2 via *in situ* iron-doping. Nat. Commun. *11*, 2034.

Gao, H., Suh, J., Cao, M.C., Joe, A.Y., Mujid, F., Lee, K.-H., Xie, S., Poddar, P., Lee, J.-U., Kang, K., et al. (2020). Tuning electrical conductance of MoS_2 monolayers through substitutional doping. Nano Lett. *20*, 4095–4101.

George, S.J., Drury, O.B., Fu, J., Friedrich, S., Doonan, C.J., George, G.N., White, J.M., Young, C.G., and Cramer, S.P. (2009). Molybdenum X-ray absorption edges from 200 to 20,000eV: the benefits of soft X-ray spectroscopy for chemical speciation. J. Inorg. Biochem. *103*, 157–167.

Guardia, L., Paredes, J.I., Munuera, J.M., Villar-Rodil, S., Ayán-Varela, M., Martínez-Alonso, A., and Tascón, J.M.D. (2014). Chemically exfoliated MoS_2nanosheets as an efficient catalyst for reduction reactions in the aqueous phase. ACS Appl. Mater. Inter. *6*, 21702–21710.

Hu, C., Yuan, C., Hong, A., Guo, M., Yu, T., and Luo, X. (2018). Work function variation of monolayer MoS_2 by nitrogen-doping. Appl. Phys. Lett. *113*, 041602.

Jariwala, D., Sangwan, V.K., Lauhon, L.J., Marks, T.J., and Hersam, M.C. (2014). Emerging device applications for semiconducting two-dimensional transition metal dichalcogenides. ACS Nano *8*, 1102–1120.

Kim, D.W., Lee, J.H., and Kim, J.K. (2020). Material aspects of triboelectric energy generation and sensors. NPG Asia Mater. *12*, 6.

Kiriya, D., Tosun, M., Zhao, P., Kang, J.S., and Javey, A. (2014). Air-stable surface charge transfer doping of MoS_2 by benzyl viologen. J. Am. Chem. Soc. *136*, 7853–7856.

Lajaunie, L., Boucher, F., Dessapt, R., and Moreau, P. (2015). Quantitative use of electron energy-loss spectroscopy Mo-M2,3 edges for the study of molybdenum oxides. Ultramicroscopy *149*, 1–8.

Lee, J., Wang, Z., Xie, H., Mak, K.F., and Shan, J. (2017). Valley magnetoelectricity in single-layer MoS_2. Nat. Mater. *16*, 887–891.

Li, J., Kang, J., Cai, Q., Hong, W., Jian, C., Liu, W., and Banerjee, K. (2017). Boosting hydrogen evolution performance of MoS_2 by band structure engineering. Adv. Mater. Inter. *4*, 1700303.

Li, L., and Li, Z. (2018). Structural phase transition barrier of N-doped MoS_2 with charge injection. Mater.Res. Express *6*, 016308.

Lim, K.-W., Peddigari, M., Park, C.H., Lee, H.Y., Min, Y., Kim, J.-W., Ahn, C.-W., Choi, J.-J., Hahn, B.-D., Choi, J.-H., et al. (2019). A high output magneto-mechano-triboelectric generator enabled by accelerated water-soluble nano-bullets for powering a wireless indoor positioning system. Energy Environ. Sci. *12*, 666–674.

Liu, L., Wu, J., Wu, L., Ye, M., Liu, X., Wang, Q., Hou, S., Lu, P., Sun, L., Zheng, J., et al. (2018). Phase-selective synthesis of 1T′ MoS_2 monolayers and heterophase bilayers. Nat. Mater. *17*, 1108–1114.

Mak, K.F., Shan, J., and Ralph, D.C. (2019). Probing and controlling magnetic states in 2D layered magnetic materials. Nat. Rev. Phys. *1*, 646–661.

Martinez, L.M., Delgado, J.A., Saiz, C.L., Cosio, A., Wu, Y., Villagrán, D., Gandha, K., Karthik, C., Nlebedim, I.C., and Singamaneni, S.R. (2018). Magnetic and electrocatalytic properties of transition metal doped MoS_2 nanocrystals. J. Appl. Phys. *124*, 153903.

Mignuzzi, S., Pollard, A.J., Bonini, N., Brennan, B., Gilmore, I.S., Pimenta, M.A., Richards, D., and Roy, D. (2015). Effect of disorder on Raman scattering of single-layer MoS_2. Phys. Rev. B *91*, 195411.

Mitterreiter, E., Schuler, B., Micevic, A., Hernangómez-Pérez, D., Barthelmi, K., Cochrane, K.A., Kiemle, J., Sigger, F., Klein, J., Wong, E., et al. (2021). The role of chalcogen vacancies for atomic defect emission in MoS_2. Nat. Commun. *12*, 3822.

Mombrú, D., Faccio, R., and Mombrú, Á.W. (2018). Possible doping of single-layer MoS_2 with Pt: a DFT study. Appl. Surf. Sci. *462*, 409–416.

Pal, B., Singh, A., G, S., Mahale, P., Kumar, A., Thirupathaiah, S., Sezen, H., Amati, M., Gregoratti, L., Waghmare, U.V., et al. (2017). Chemically exfoliated MoS_2 layers: spectroscopic evidence for the semiconducting nature of the dominant trigonal metastable phase. Phys. Rev. B *96*, 195426.

Park, T.-E., Suh, J., Seo, D., Park, J., Lin, D.-Y., Huang, Y.-S., Choi, H.-J., Wu, J., Jang, C., and Chang, J. (2015). Hopping conduction in p-type MoS_2 near the critical regime of the metal-insulator transition. Appl. Phys. Lett. *107*, 223107.

Parmar, S., Biswas, A., Kumar Singh, S., Ray, B., Parmar, S., Gosavi, S., Sathe, V., Janay Choudhary, R., Datar, S., and Ogale, S. (2019). Coexisting 1T/2H polymorphs, reentrant resistivity behavior, and charge distribution in MoS_2—hBN 2D/2D composite thin films. Phys. Rev. Mater. *3*, 074007.

Parmar, S., Biswas, A., Ray, B., Gosavi, S., Datar, S., and Ogale, S. (2021a). Stabilizing metastable polymorphs of van der Waals solid MoS_2 on single crystal oxide substrates: exploring the possible role of surface chemistry and structure. J. Phys. Chem. C *125*, 11216–11224.

Parmar, S., Das, T., Biswas, A., Ray, B., Debnath, B., Gosavi, S., Shanker, G.S., Datar, S., Chakraborty, S., and Ogale, S. (2021b). N, H dual-doped black anatase TiO_2 thin films toward significant self-activation in electrocatalytic hydrogen evolution reaction in alkaline media. Adv. Energy Sustainability Res. *3*, 2100137. https://doi.org/10.1002/aesr.202100137.

Reinholdt, P., Vidal, M.L., Kongsted, J., Iannuzzi, M., Coriani, S., and Odelius, M. (2021). Nitrogen K-edge X-ray absorption spectra of ammonium and ammonia in water solution: assessing the performance of polarizable embedding coupled cluster methods. J. Phys. Chem. Lett. *12*, 8865–8871.

Rosa, C.J.L.d.l., Phillipson, R., Teyssandier, J., Adisoejoso, J., Balaji, Y., Huyghebaert, C., Radu, I., Heyns, M., Feyter, S.D., and Gendt, S.D. (2016). Molecular doping of MoS_2 transistors by self-assembled oleylamine networks. Appl. Phys. Lett. *109*, 253112.

Sebastian, A., Pendurthi, R., Choudhury, T.H., Redwing, J.M., and Das, S. (2021). Benchmarking monolayer MoS_2 and WS_2 field-effect transistors. Nat. Commun. *12*, 693.

Seol, M., Kim, S., Cho, Y., Byun, K.-E., Kim, H., Kim, J., Kim, S.K., Kim, S.-W., Shin, H.-J., and Park, S. (2018). Triboelectric series of 2D layered materials. Adv. Mater. *30*, 1801210.

Serna, M.I., Yoo, S.H., Moreno, S., Xi, Y., Oviedo, J.P., Choi, H., Alshareef, H.N., Kim, M.J., Minary-Jolandan, M., and Quevedo-Lopez, M.A. (2016). Large-area deposition of MoS_2 by pulsed laser deposition with *in situ* thickness control. ACS Nano *10*, 6054–6061.

Serrao, C.R., Diamond, A.M., Hsu, S.-L., You, L., Gadgil, S., Clarkson, J., Carraro, C., Maboudian, R., Hu, C., and Salahuddin, S. (2015). Highly crystalline MoS_2 thin films grown by pulsed laser deposition. Appl. Phys. Lett. *106*, 052101.

Shin, B., Zhu, Y., Bojarczuk, N.A., Chey, S.J., and Guha, S. (2012). Control of Interfacial $MoSe_2$ Layer Thickness in $CuZnSnSe_4$ Thin Film Solar Cell: 8.9% power conversion efficiency with a TiN diffusion barrier. Appl. Phys. Lett. *161*, 053903.

Siegel, G., Subbaiah, Y.P.V., Prestgard, M.C., and Tiwari, A. (2015). Growth of centimeter-scale atomically thin MoS_2 films by pulsed laser deposition. APL Mater. *3*, 056103.

Tang, J., Wei, Z., Wang, Q., Wang, Y., Han, B., Li, X., Huang, B., Liao, M., Liu, J., Li, N., et al. (2020). *In Situ* oxygen doping of monolayer MoS_2 for novel electronics. Small *16*, 2004276.

Tang, Q., and Jiang, D.-e. (2015). Stabilization and band-gap tuning of the 1T-MoS_2 monolayer by covalent functionalization. Chem. Mater. *27*, 3743–3748.

Tao, J., Chai, J., Lu, X., Wong, L.M., Wong, T.I., Pan, J., Xiong, Q., Chi, D., and Wang, S. (2015). Growth of wafer-scale MoS_2 monolayer by magnetron sputtering. Nanoscale *7*, 2497–2503.

Tao, J., Chai, J.W., Zhang, Z., Pan, J.S., and Wang, S.J. (2014). The energy-band alignment at molybdenum disulphide and high-k dielectrics interfaces. Appl. Phys. Lett. *104*, 232110.

Wang, H., Tran, D., Qian, J., Ding, F., and Losic, D. (2019a). MoS_2/Graphene composites as promising materials for energy storage and conversion applications. Adv. Mater. Inter. *6*, 1900915.

Wang, J., Zhou, Q., Lu, Z., Gui, Y., and Zeng, W. (2019b). Adsorption of H_2O molecule on TM (Au, Ag) doped-MoS_2 monolayer: a first-principles study. Phys. E Low-dimens. Syst. Nanostruct. *113*, 72–78.

Wang, S., Yu, H., Zhang, H., Wang, A., Zhao, M., Chen, Y., Mei, L., and Wang, J. (2014). Broadband few-layer MoS_2saturable absorbers. Adv. Mater. *26*, 3538–3544.

Yang, L., Majumdar, K., Liu, H., Du, Y., Wu, H., Hatzistergos, M., Hung, P.Y., Tieckelmann, R., Tsai, W., Hobbs, C., et al. (2014). Chloride molecular doping technique on 2D materials: WS_2 and MoS_2. Nano Lett. *14*, 6275–6280.

Yang, Q., Wang, Z., Dong, L., Zhao, W., Jin, Y., Fang, L., Hu, B., and Dong, M. (2019). Activating MoS_2 with super-high nitrogen-doping concentration as efficient catalyst for hydrogen evolution reaction. J. Phys. Chem. C *123*, 10917–10925.

Zhang, X.-X., Lai, Y., Dohner, E., Moon, S., Taniguchi, T., Watanabe, K., Smirnov, D., and Heinz, T.F. (2019). Zeeman-induced valley-sensitive photocurrent in monolayer MoS_2. Phys. Rev. Lett. *122*, 127401.

Zhang, X., Liao, Q., Kang, Z., Liu, B., Liu, X., Ou, Y., Xiao, J., Du, J., Liu, Y., Gao, L., et al. (2021). Hidden vacancy benefit in monolayer 2D semiconductors. Adv. Mater. *33*, 2007051.

Zhao, W., Pan, J., Fang, Y., Che, X., Wang, D., Bu, K., and Huang, F. (2018). Metastable MoS_2: crystal structure, electronic band structure, synthetic approach and intriguing physical properties. Chemistry *24*, 15942–15954.

Zhou, Y., Kiriya, D., Haller, E.E., Ager, J.W., Javey, A., and Chrzan, D.C. (2016). Compliant substrate epitaxy: Au on MoS_2. Phys. Rev. B *93*, 054106.

Zou, J., Li, F., Bissett, M.A., Kim, F., and Hardwick, L.J. (2020). Intercalation behaviour of Li and Na into 3-layer and multilayer MoS_2 flakes. Electrochim.Acta *331*, 135284.

STAR★METHODS

KEY RESOURCES TABLE

REAGENT or RESOURCE	SOURCE	IDENTIFIER
Chemicals, peptides, and recombinant proteins		
Molybdenum di sulfide (99.9%)	Sigma-Aldrich	CAS# 1317-33-5
Aceton, 99.9%	Sigma Aldrich	CAS# 67-64-1
c-Al_2O_3 Substrate (99.99%)	MTI	Product# ALC25D05C1
ITO PET sheets	Sigma Aldrich	Product# 639303-1EA
Aluminum Foil Tape	3M	Product# 3363
Copper Foil Tape	3M	Product# 1182
Microfiber paper	Sigma Aldrich	Product# WHA2200070
Double sided tape	3M	Product# GPH-110GF

RESOURCE AVAILABILITY

Lead contact

Further information and requests for resources and reagents should be directed to and will be fulfilled by the lead contact, Satishchandra Ogale (satishogale@iiserpune.ac.in)

Materials availability

This work is an experimental study of thin-film growth and nanogenerators and there is no new code generated.

Data and code availability

- All data reported in this paper will be shared by the lead contact upon request.
- No new code was generated during the course of this study.
- Any additional information required to reanalyze the data reported in this paper is available from the lead contact upon request.

EXPERIMENTAL MODEL AND SUBJECT DETAILS

Molybdenum di-sulfide (MoS_2, 99.9%) was purchased from Sigma-Aldrich. The chemical was used without further purification. Ammonia-Argon gas cylinder (30% Ammonia Bal Argon Pressure 20 Bar/cm^2 Purity-99.9%) was used for the deposition of $MoS_{2-x}N_x$ thin films. The *c*-Al_2O_3 substrates were cut into 5x5 mm^2 area using diamond cutter and sintered at 1000ºC to obtain atomically flat substrate followed by washing away residual dust/particle with sonicating under acetone and deionized water at room temperature for 15 min each. They were then blow dried in Ar air before loading into the PLD chamber. The ITO coated PET was directly used for deposition without any treatment.

METHOD DETAILS

$MoS_{2-x}N_x$ thin-film growth

In this work, we have grown 50 nm thin-films of $MoS_{2-x}N_x$ under NH_3 pressures of 1 mTorr, 10 mTorr, 100 mTorr, and 300 mTorr respectively by Pulsed Laser Deposition (PLD) (KrF, λ = 248). Here we have used *c*-Al_2O_3 substrates for the detailed characterization and ITO coated PET for nanogenerator application. The $MoS_{2-x}N_x$ films were deposited at 400°C and 150°C on *c*-Al_2O_3 and ITO-coated PET substrates, respectively. To make the *c*-Al_2O_3 substrate atomically flat, the annealing treatment was given at 1000°C for 1 h in air before the deposition. The distance between the polycrystalline MoS_2target to the substrate was ~40 mm. The substrate temperature was 400°C for all depositions under ammonia-argon gas mixture (30% ammonia) at 5 Hz frequency by using 1.5 J/cm^2 laser energy density. Pristine MoS_2 films were deposited under vacuum with the base pressure of 10^{-6} mbar. All films were cooled down naturally.

Structural and chemical characterizations

Raman spectra for all MoS_2 thin-film samples were recorded at ~2.33 eV (532 nm) excitation energy laser. Atomic force microscopy (AFM) topography images of thin films were taken using Nanosurf AFM (Switzerland). X-ray photoelectron spectroscopy (XPS) was performed in an ultra-high vacuum chamber ($2x10^{-9}$ mBar) by using an Al Kαx-ray source with 6 mA beam current on a Thermo-Fisher Scientific Instrument, UK, where beam spot size on the thin-film samples were ~400 μm. High-resolution transmission electron microscopy (HRTEM) images were recorded using UHR FEG-TEM microscopic instrument, operating at 200 kV accelerating voltage. To record the absorption spectrum of $MoS_{2-x}N_x$ thin film, an ultraviolet-visible (UV–vis) spectrophotometer (LAMBDA 950, PerkinElmer) was used. Field emission scanning electron microscopy (FESEM) images of the electrodes were recorded using a JEM-2100F (JEOL, Japan) instrument.

X-ray absorption spectroscopy measurement of N K-edges was collected in total electron yield (TEY) mode of $MoS_{2-x}N_x$ characterization was done using synchrotron radiation source at RRCAT, Indore at 'polarized light soft X-ray absorption spectroscopy beamline' (BL-01) in INDUS-2, respectively. Before recording the XAS spectra, the thin film surface was sputtered using high energy Argon ions inside the chamber where base pressure was maintained at ~1×10^{-10} mbar in order to remove any surface contamination.

Electrical characterization

Electrical measurements were performed in standard AC transport four-probe method by using a Quantum Design Physical Property Measurement System (PPMS), over the temperature range of T = 5-300 K, where the dimensions of MoS_2 and $MoS_{2-x}N_x$ film was 2x5 mm^2.

Nanogenerator output performance

Keithley multimeter (DMM7510 7.5 multimeter) was used to measure open circuit voltage at 10 MΩ input impedance at 10 N impact force with 21 Hz frequency. For the impact force and frequency source, we used home-made modified sewing machine setup. We measured force using PASPORT Force Sensor. Voltage and current were also measured on Keithley multimeter (DMM7510 7.5 multimeter) with variable resistance.

QUANTIFICATION AND STATISTICAL ANALYSIS

The TENG data were collected on a Kickstart, an oscilloscope testing system (DMM7510). Figures were produced by Origin from the raw data.

ADDITIONAL RESOURCES

Any additional information about the thin-film fabrication, TENG fabrication, tests and data reported in this paper is available from the lead contact on request.